The Lyα luminosity function at z = 5.7 − 6.6 and the steep drop of the faint end: implications for reionization

Sérgio Santos[1,2,3]★, David Sobral[3,4] & Jorryt Matthee[4]

[1] *Instituto de Astrofísica e Ciências do Espaço, Universidade de Lisboa, OAL, Tapada da Ajuda, PT1349-018 Lisboa, Portugal*
[2] *Departamento de Física, Faculdade de Ciências, Universidade de Lisboa, Edifício C8, Campo Grande, PT1749-016 Lisbon, Portugal*
[3] *Department of Physics, Lancaster University, Lancaster, LA1 4YB, UK*
[4] *Leiden Observatory, Leiden University, P.O. Box 9513, NL-2300 RA Leiden, The Netherlands*

23 August 2016

ABSTRACT

We present new results from the widest narrow band survey search for Lyα emitters at $z = 5.7$, just after reionization. We survey a total of $7 \deg^2$ spread over the COSMOS, UDS and SA22 fields. We find over 11,000 line emitters, out of which 514 are robust Lyα candidates at $z = 5.7$ within a volume of 6.3×10^6 Mpc³. Our Lyα emitters span a wide range in Lyα luminosities, from faint to bright ($L_{Ly\alpha} \sim 10^{42.5-44}$ erg s⁻¹) and rest-frame equivalent widths ($EW_0 \sim 25 - 1000$ Å) in a single, homogeneous data-set. By combining all our fields we find that the faint end slope of the $z = 5.7$ Lyα luminosity function is very steep, with $\alpha = -2.3^{+0.4}_{-0.3}$. We also present an updated $z = 6.6$ Lyα luminosity function, based on comparable volumes and obtained with the same methods, which we directly compare with that at $z = 5.7$. We find a significant decline of the number density of faint Lyα emitters from $z = 5.7$ to $z = 6.6$ (by 0.5 ± 0.1 dex), but no evolution at the bright end/no evolution in L^*. Faint Lyα emitters at $z = 6.6$ show much more extended haloes than those at $z = 5.7$, suggesting that neutral Hydrogen plays an important role, increasing the scattering and leading to observations missing faint Lyα emission within the epoch of reionization. All together, our results suggest that we are observing patchy reionization which happens first around the brightest Lyα emitters, allowing the number densities of those sources to remain unaffected by the increase of neutral Hydrogen fraction from $z \sim 5$ to $z \sim 7$.

Key words: galaxies: high-redshift – galaxies: luminosity function – cosmology:observations – cosmology: dark ages, reionization, first stars.

1 INTRODUCTION

During the past two decades, considerable progress has been made in understanding the distant/early Universe (see reviews by e.g. Robertson et al. 2010; Dunlop et al. 2012; Madau & Dickinson 2014). Currently, the samples of $z > 6$ candidates are mostly composed by rest-frame ultra-violet (UV) selected galaxies obtained from extremely deep surveys with the Hubble Space Telescope (e.g. Bouwens et al. 2015; Finkelstein et al. 2015). However, spectroscopy and multi-wavelength follow-up (e.g. with ALMA; Ouchi et al. 2013; Watson et al. 2015; Capak et al. 2015; Maiolino et al. 2015) of these sources still remains very limited as most candidates are too faint for a detailed analysis with current instrumentation (see also Dunlop et al. 2016). Alternatively, emission lines can be used to search for high-redshift galaxies to directly select galaxies by their brightest features, including

several rest-frame optical and UV lines (e.g. Ouchi et al. 2008; Sobral et al. 2013; Khostovan et al. 2015, 2016), allowing for efficient follow-up strategies.

The Lyman-α (Lyα) emission line (rest-frame 1215.67 Å) is emitted by both young star-forming galaxies and active galactic nuclei/quasars, being intrinsically the strongest emission line in the rest-frame optical to UV (e.g. Partridge & Peebles 1967; Pritchet 1994). As Lyα is redshifted into optical wavelengths (it can be observed from the ground at $z \approx 2 - 7$), many other strong lines are redshifted out of even the near-infrared (see e.g. Ly et al. 2007, 2011; Hayes et al. 2010; Sobral et al. 2013), making Lyα one of the only available means of spectroscopic confirmation, along with other weaker high ionisation UV lines (e.g. Sobral et al. 2015; Stark et al. 2016).

Several approaches have been used to find and study Lyα emitters, including blind spectroscopy (e.g. Martin & Sawicki 2004; Stark et al. 2007; Rauch et al. 2008; Sawicki et al. 2008; Bayliss et al. 2010; Cassata et al. 2011),

★ E-mail: ssantos@oal.ul.pt

narrow band surveys (e.g. Cowie & Hu 1998; Rhoads et al. 2000, 2003; Malhotra & Rhoads 2004; Taniguchi et al. 2005; Shimasaku et al. 2006; Westra et al. 2006; Iye et al. 2006; Nilsson et al. 2007; Murayama et al. 2007; Ouchi et al. 2008, 2010; Sobral et al. 2009; Hu et al. 2010; Kashikawa et al. 2011; Shibuya et al. 2012; Konno et al. 2014; Matthee et al. 2014, 2015) and Integral Field Unit (IFU) observations (e.g. Blanc et al. 2011; Adams et al. 2011; van Breukelen et al. 2005; Bacon et al. 2015; Karman et al. 2015). Blind spectroscopy and IFU surveys can be very efficient at probing ultra-low luminosity sources at a variety of redshifts, but the current small volumes probed make them unable to reach even L^* sources, as the rarer (brighter) sources have number densities several times smaller that these studies can reach. Wide narrow band surveys can be very competitive at efficiently probing large volumes at specific look-back times, and can be used to study a much larger luminosity range. For example, one MUSE pointing (e.g. Bacon et al. 2015) probes a volume of $\sim 10^3\,\mathrm{Mpc}^3$ for $z \sim 3-6$, while one Subaru Suprime-Cam pointing with a typical narrow band filter probes a volume of $\sim 10^5\,\mathrm{Mpc}^3$ (Hyper Suprime-Cam covers a volume ~ 7 times larger per pointing). Typically, narrow band surveys have targeted a maximum of $\sim 1\,\mathrm{deg}^2$ areas, corresponding to maximum volumes of $\sim 10^6\,\mathrm{Mpc}^3$ (e.g. Ouchi et al. 2008, 2010), but the next generation of surveys are now starting to probe much larger volumes (e.g. Matthee et al. 2015; Hu et al. 2016).

Due to its resonant nature, Lyα photons are easily scattered by neutral hydrogen (and also easily absorbed by dust; e.g. Hayes et al. 2011). As a consequence, the observability of Lyα can in principle be used as a probe of the neutral state of the inter-galactic medium (IGM) during the epoch of reionization (e.g. Fontana et al. 2010; Caruana et al. 2012; Schenker et al. 2012; Ono et al. 2012; Caruana et al. 2014; Dijkstra 2014; Pentericci et al. 2014; Schmidt et al. 2016). However, in order to interpret Lyα observations (such as the distribution of equivalent widths, the fraction of UV selected galaxies with strong Lyα, or the evolution of the number density of Lyα emitters) as consequences of reionization, one needs to accurately understand the contribution from potentially varying intrinsic inter-stellar medium (ISM) properties such as the Lyα escape fraction (c.f. Matthee et al. 2016a), overdensities of galaxies (e.g. Castellano et al. 2016) or selection biases in UV selected galaxy samples (c.f. Oesch et al. 2015; Zitrin et al. 2015; Stark et al. 2016). Therefore, it is important to have a clear understanding of Lyα with only little influence from the IGM at $z \approx 6$, when reionization is close to complete and the fraction of neutral hydrogen becomes extremely low (Fan et al. 2006; Becker et al. 2015).

Previous studies found that the Lyα luminosity function (LF) seems to have little evolution at $z \sim 3-6$ (e.g. Ouchi et al. 2008). In contrast, the UV LF of Lyman-break galaxies (LBGs) strongly decreases for higher redshifts (e.g. Bouwens et al. 2015; Finkelstein et al. 2015). This difference in evolution is likely explained by an evolving escape fraction of Lyα photons, likely due to a lower dust content, younger stellar populations, lower metallicities and/or a combination of related phenomena. This is consistent with the observation that the fraction of LBGs with strong Lyα emission increases up to $z = 6$ (e.g. Stark et al. 2010; Cassata et al. 2015). At $z > 6$ the number density of faint Lyα emitters (LAEs) is found to decline with redshift (Ouchi et al. 2010; Konno

et al. 2014), likely due to reionization not being fully completed. However, by using the largest Lyα survey at $z \sim 7$ ($\sim 5\,\mathrm{deg}^2$), Matthee et al. (2015) show that the strong decrease/evolution in the number density of LAEs happens pre-dominantly at relative faint Lyα luminosities, while the bright end (with luminosities $\mathrm{L_{Ly\alpha}} > 10^{43}\,\mathrm{erg\,s^{-1}}$) may not evolve at all. Matthee et al. (2015) finds that bright LAEs at $z = 6.6$ are much more common than previously thought, with spectroscopic confirmation presented in Sobral et al. (2015), and with independent studies finding consistent results (see e.g. Hu et al. 2016). However, one strong limitation in interpreting the potential evolution from $z = 6.6$ to $z = 5.7$ is the lack of comparably large $\sim 5-10\,\mathrm{deg}^2$, multiple field surveys that can both trace a large enough number of bright sources and overcome cosmic variance.

In this work, we present the largest Lyα narrow band survey at $z = 5.7$, covering a total of $\sim 7\,\mathrm{deg}^2$ ($\sim 10^7\,\mathrm{Mpc}^3$). Previous studies have never probed beyond $2\,\mathrm{deg}^2$ (e.g. Murayama et al. 2007; Ouchi et al. 2008; Hu et al. 2010), and have mostly focused on specific, single fields. Here we take advantage of previous data and add further $\sim 4\,\mathrm{deg}^2$ of unexplored data. We also re-analyse the $z = 6.6$ luminosity function presented in Matthee et al. (2015).

We structure this paper as follows: Section 2 presents the observations and data reduction. Section 3 explains the selection of line emitters and Lyα emitters at $z = 5.7$. In Section 4 we present the method and procedures adopted to construct the $z = 5.7$ and $z = 6.6$ Lyα LFs. We present our results in Section 5, including a comparison with previous surveys. Section 6 discusses the results in the context of predicted effects from reionization. Finally Section 7 presents the conclusions of this paper.

Throughout this work we use a ΛCDM cosmology with $\mathrm{H_0} = 70\,\mathrm{km\,s^{-1}\,Mpc^{-1}}$, $\Omega_M = 0.3$ and $\Omega_\Lambda = 0.7$. All magnitudes in this paper are presented in the AB system. At $z = 5.7$, $1''$ corresponds to 5.9 kpc.

2   OBSERVATIONS AND DATA REDUCTION

2.1   Observations

We have reduced and analyzed raw archival NB816 data in the COSMOS, UDS and SA22 fields. We use these three fields as they are completely independent (preventing any possible bias from probing the same region of the sky) and far enough from the galactic plane (avoiding bright foreground stars and dust). Additionally, the available deep multi-wavelength coverage (including optical and near infrared) allows a robust selection of candidates and identification of any lower redshift interlopers.

The NB816 filter has a central wavelength of $8150\,\mathrm{\mathring{A}}$ and a full width at half maximum (FWHM) of $120\,\mathrm{\mathring{A}}$. NB816 is contained within the red wing of the broad band filter i (see Figure 1). All NB816 data were collected with the Suprime-Cam instrument from the Subaru Telescope (Miyazaki et al. 2002). Suprime-Cam has ten 2048x4096 CCDs arranged in a 5×2 pattern, with a corresponding field of view of $\sim 0.25\,\mathrm{deg}^2$. We use a total of 30 of these pointings. Suprime-cam images have a pixel scale of $0.20''\,\mathrm{pix}^{-1}$.

We retrieved all publicly available raw NB816 data for

Table 1. Our NB816 data in the COSMOS, UDS and SA22 fields. The SA22 field was separated into two sub-fields, deep and wide, according to its significantly different NB816 depth. R.A. and Dec. are the central coordinates of the fields. FWHM is the average value for the seeing and is similar across our entire coverage. The NB816 depth is the 2σ depth measured in $2''$ apertures. Note that the quoted area already takes into account the removed/masked regions which are not used in this paper.

Field	R.A. (J2000)	Dec. (J2000)	Area (deg^2)	FWHM ($''$)	NB816 depth (2σ, $2''$)
COSMOS	10 00 00	+02 10 00	2.00	0.7	26.2
UDS	02 18 00	−05 00 00	0.85	0.7	26.1
SA22-deep	22 18 00	+00 20 00	0.55	0.7	26.1
SA22-wide	22 15 00	+00 50 00	3.60	0.5	25.0
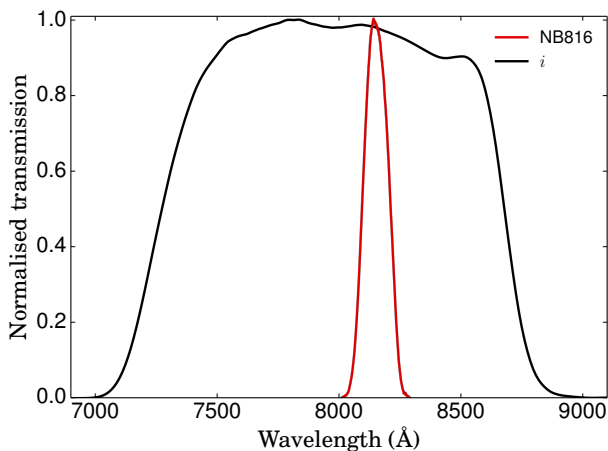
Figure 1. Normalised filter profiles of the NB816 and the i band filters used in this study. We note that the shown i band is for Subaru's Suprime-Cam after the upgrade to red sensitive CCDs, such that its peak is slightly shifted towards the red compared to the CFHT MegaCam i band used for SA22. Our NB correction in Section 2.4.1 takes this into account. NB816 is contained slightly red from the center of i. The NB816 filter is located in a wavelength region free of strong atmospheric OH lines.

the UDS and SA22 fields from the SMOKA Archive[1]. Fully reduced COSMOS NB816 images (original PSF) were retrieved from the COSMOS Archive[2] (Taniguchi et al. 2007; Capak et al. 2007).

We split SA22 data into two different sub-fields (SA22-deep and SA22-wide), which differ in depth by ≈ 1 mag and in area by a factor of ≈ 6.6. SA22-wide contains the largest area (larger than COSMOS and UDS combined). Narrow band observations are summarized in Table 1.

Previous studies have separately used NB816 data in COSMOS (Murayama et al. 2007), UDS/SXDF (Ouchi et al. 2008) and SA22-deep (~ 0.4 deg^2; Hu et al. 2010). We note that while we explore new data and provide the largest survey of its kind, we are able to reproduce individual results from the literature using our own analysis. A comparison between our findings and previous studies is presented in Section 4.

2.2 Data reduction

We used the Subaru data reduction pipelines (SFRED and SFRED2; Ouchi et al. 2004) to reduce the NB816 data. The data reduction follows the same procedure as detailed in e.g. Matthee et al. (2015) and we refer the reader to that study for more details. Briefly, the reduction steps include: overscan and bias subtraction, flat fielding, point spread function homogenisation, sky background subtraction and bad pixel masking. After these steps, we apply an astrometric calibration using SCAMP (Bertin 2006) to correct astrometric distortions. The software matches our images with the 2MASS catalog in the J band (Skrutskie et al. 2006) and fits polynomial functions that correct for any distortions along the CCD.

We calibrated the photometry in our data by matching relatively bright, un-saturated stars and galaxies to public catalogues for COSMOS (Laigle et al. 2016), UDS (Cirasuolo et al. 2007) and SA22 (Sobral et al. 2013, 2015; Matthee et al. 2014) using STILTS (Taylor 2006). NB816 images were calibrated using i band photometry, but a further correction to this calibration was applied in Section 2.4.1. Co-added stacks of NB816 exposures were obtained using the SWARP software (Bertin et al. 2002).

We masked low quality regions, bright haloes around bright stars, diffraction patterns and low S/N regions due to dithering strategy (particularly important in SA22-wide). We also removed regions with low quality or absent i band coverage, regardless of the quality of the narrow band.

We note that our masking is very conservative and, consequently, a relatively large area is removed from our study (hundreds of arcmin^2), but that is still only a small fraction of our total area. After masking low quality regions, our NB816 coverage contains a total area of 7 deg^2 (Figure 2), corresponding to a comoving volume of 6.3×10^6 Mpc^3 at $z = 5.7$. All areas and volumes used and mentioned in this paper take into account these masks, unless stated otherwise.

Finally, we measure the depth of our images using randomly placed $2''$ apertures. In each image, we place 200,000 empty apertures in random positions. The average results per field are given in Table 1.

2.3 Multi-wavelength imaging

A large collection of multi-wavelength data are publicly available for our entire coverage. For the COSMOS field, we use optical $BVgriz$ data taken with the Sub-
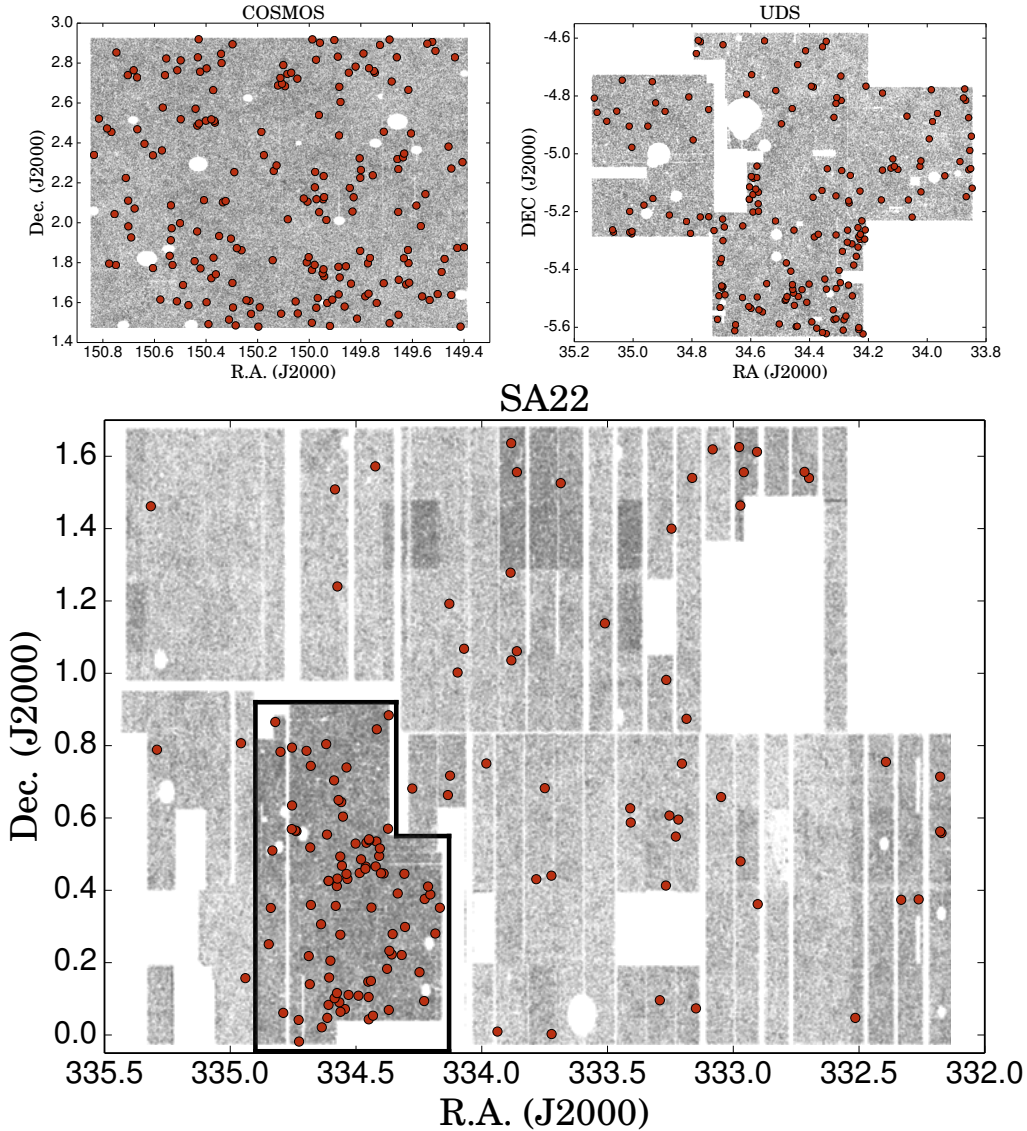
---

[1] http://smoka.nao.ac.jp/
[2] http://irsa.ipac.caltech.edu/data/COSMOS/

Figure 2. The spatial distribution of sources in the COSMOS, UDS and SA22 fields. Grey dots indicate all detections and red circles identify our $z = 5.7$ Lyα emitter candidates. A black line contour identifies SA22-deep, the deepest region in the SA22 field. The figure also highlights the regions masked due to bright stars, bad regions and/or low S/N due to dither strategy. It can be seen that UDS, COSMOS and SA22-deep are the deepest regions with a high concentration of sources and candidate LAEs.

Table 2. Multi-wavelength depths (2σ; measured in $2''$ empty apertures) for the available broad-band filters across all three fields.

Field	Broad band filters	Broad band depth (2σ, $2''$)
COSMOS	$BVgrizYJHK$	27.6, 27.0, 27.1, 27.0, 26.6, 25.7, 25.3, 24.6, 25.0, 24.7
UDS	$BVrizJK$	27.5, 27.2, 27.0, 26.8, 27.0, 25.3, 24.8
SA22	$ugrizJK$	26.2, 26.5, 25.9, 25.6, 24.5, 24.3, 23.8

aru/SuprimeCam (Taniguchi et al. 2007; Capak et al. 2007), retrieved from the COSMOS Archive and NIR *YHJK* data from UltraVISTA DR2 (McCracken et al. 2012), taken with VISTA/VIRCAM. For the UDS field, we use optical *BVriz* data from SXDF (Furusawa et al. 2008) and NIR *JHK* data from UKIDSS (Lawrence et al. 2007). For the SA22 field we use optical *ugriz* data from CFHTLS[3], taken with the Mega-Cam (Boulade et al. 2003) and NIR *JK* data from UKIDSS DXS (Warren et al. 2007), taken with UKIRT/WFCAM (Casali et al. 2007). All data which were not taken with the Subaru/SuprimeCam were degraded to a pixel scale of
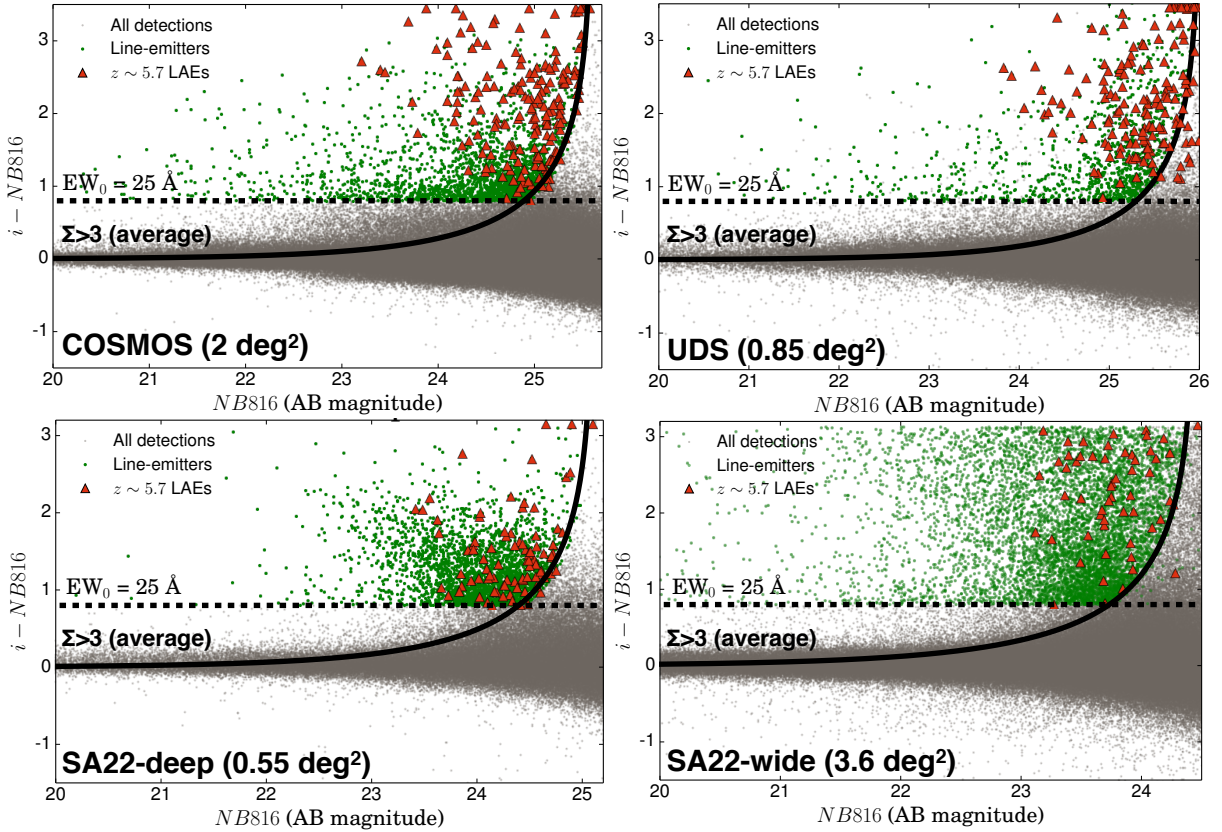
---

[3] http://www.cfht.hawaii.edu/Science/CFHTLS/

Figure 3. Narrow band excess diagram for COSMOS, UDS and SA22. We plot narrow band excess (i broad band magnitude minus NB816 magnitude) versus narrow band NB816 magnitude. Grey points represent all detections after masking, removal of sources with non-physical narrow band and cosmic rays. Green points represent line-emitters, obtained by applying the EW and Σ cuts described in Section 3. For visual reference, we collapsed the points with no i detection in the top region of the plots. The Σ line shown in this figure is the median value from small sub-fields which we created inside each field.

$0.20'' \, \mathrm{pix}^{-1}$ using SWARP. A summary of the available filters for each field and their photometric depth is shown in Table 2.

2.4 NB816 catalogue

The extraction of sources was conducted using SEXTRAC-TOR (Bertin & Arnouts 1996) in dual extraction mode, using NB816 as the detection image.

2.4.1 Narrow band magnitude correction

The NB816 filter is located slightly to the red of the Sub-aru Suprime-cam i filter (with red sensitive CCDs) with a separation of $\approx 180 \, \text{Å}$ between the center of the two filters. Calibrating the narrow band magnitude directly to the i band may result in an offset in the magnitudes, particularly for sources with strong colours. We correct the narrow band magnitudes by summing a small correction factor which is estimated from the color of the two adjacent broad bands, i and z. To compute this correction, we use sources with i, z and NB816 magnitudes between 19 and 24 (not saturated and with high enough S/N). The correction has the following expression:

$$NB_{corrected} = NB + 0.4 \times (i - z), \qquad (1)$$

where NB, i and z are the $2''$ magnitudes in the respective bands and $NB_{corrected}$ is the corrected NB816 magnitude. We apply this correction to sources with i and z detections. For the remaining sources, we apply a median correction of $+0.20$. As a result of this correction, there is less scatter in the excess diagram (Figure 3). The correction also corrects for the fact that the CFHT MegaCam i band is slightly bluer than Suprime-cam's i band, because this slightly different i band will result in slightly different $i - z$ colours.

Our narrow band correction is an alternative to the correction applied in Murayama et al. (2007) who used a corrected broad band obtained from an iz interpolation. Our narrow band correction corresponds to a $BB_{corrected} = 0.6i + 0.4z$ which is fully consistent with their interpolation.

2.4.2 Removal of sources with non-physical narrow band detection

The wavelengths covered by NB816 are contained inside the i band coverage. This means that sources with NB816 detection should be detected in i as long as the i image is deep enough. For each source we compute the expected i magnitude if it only had emission inside NB816. If the measured i magnitude of a source is fainter than this value and the depth of the i image is sufficient to detect it, we remove it from our sample. This step mainly removes variable

sources (such as supernovae and moving sources) and spurious sources that are detected only in the narrow band images and sources with boosted narrow band emission from e.g. diffraction patterns.

2.4.3 Cosmic ray removal

Cosmic rays may become artefacts in images. This problem can be avoided through stacking of several frames. However, in our shallower SA22-wide data, the small number of frames causes a less efficient removal of such artefacts during stacking. We created an automated procedure to identify and remove cosmic rays from our sample.

For each source detected in the NB816 imaging we measure the standard deviation in boxes of 5×5 pixels around each source. Cosmic rays can be easily identified by their high standard deviation, several times higher than any real source. We apply a cautious cut to make sure we do not lose any real sources. Since we were cautious with this step, we also visually inspect all the final LAE candidates to identify any cosmic ray that was not excluded.

3   SELECTING NB816 LINE EMITTERS

For the selection of line-emitters, we apply similar criteria to e.g. Sobral et al. (2013) and Matthee et al. (2015), relying on two parameters: equivalent width (EW) and Sigma (Σ). The equivalent width is the ratio between the flux of an emission line and the continuum flux. It can be expressed as:

$$EW_{obs} = \Delta \lambda_{NB} \frac{f_{NB} - f_{BB}}{f_{BB} - f_{NB}(\Delta \lambda_{NB}/\Delta \lambda_{BB})}, \qquad (2)$$

where $\Delta \lambda_{NB}$ and $\Delta \lambda_{BB}$ are the FWHM of the narrow band and broad band filters ($\Delta \lambda_{NB816}$ =120 Å; $\Delta \lambda_i$ =1349 Å) and f_{NB} and f_{BB} are the flux densities measured in the two filters.

The second parameter, Sigma (Σ, e.g. Bunker et al. 1995), is used to assure that the excess of the NB816 relative to the broad-band is significantly above the noise. It can be written as (Sobral et al. 2013):

$$\Sigma = \frac{1 - 10^{-0.4(BB-NB)}}{10^{-0.4(ZP-NB)}\sqrt{rms_{BB}^2 + rms_{NB}^2}} \qquad (3)$$

where BB and NB are the broad band and the corrected narrow band magnitudes (in this case, NB816 and i), ZP is the zero-point of the image (set to 30) and rms is the root-mean-square of the background of the respective image.

To select our sample of line-emitters, we apply the following selection criteria:

- $i - NB816 > 0.8$
- $\Sigma > 3$

The narrow band excess criteria $i - NB816 > 0.8$ corresponds to a rest-frame EW of 25 Å for a $z = 5.7$ LAE. This cut is similar to the one used by Hu et al. (2010) and Matthee et al. (2015) for $z = 6.6$ but slightly lower than e.g. Ouchi et al. (2008) ($i - NB816 > 1.2$) and Taniguchi et al. (2005) ($i - NB816 > 1$).

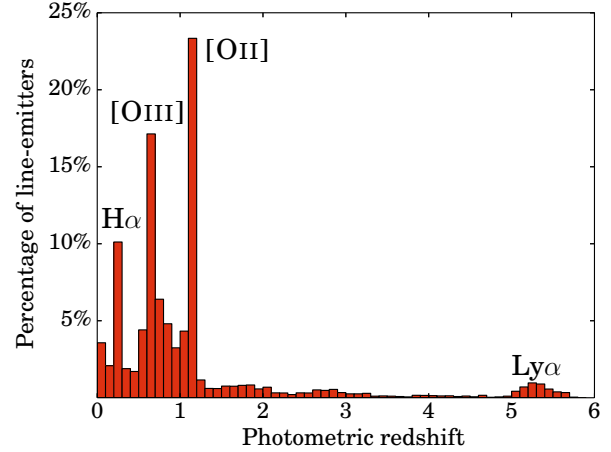We present the narrow band excess diagram in Figure 3,

Figure 4. Distribution of photometric redshifts of line-emitters selected in COSMOS, UDS and SA22 by using a simple selection criteria of $i - NB186 > 0.25$ and $\Sigma > 3$. The peaks are consistent with line emission at specific wavelengths. Annotations indicate the redshifts where we expect major emission lines (Hα at $z \sim 0.2$, [OIII] at ~ 0.6, [OII] at $z \sim 1.2$ and Lyα at $z = 5.7$).

highlighting our sample of line-emitters. With our selection criteria we identify over 11,000 candidate line emitters.

3.1   Photometric and spectroscopic redshifts

In order to explore the nature of the line-emitters, we have used accurate photometric redshifts and a large compilation of spectroscopic redshifts: Laigle et al. (2016) for COSMOS, Cirasuolo et al. (2007) for UDS and a combination of Kim et al. (2015), Matthee et al. (2014) and Sobral et al. (2015) for SA22. We retrieve ~ 5000 emitters with either available photometric or spectroscopic redshift. Figure 4 presents the distribution of photometric redshifts of our sample of line emitters. Even though our high EW cut is tuned to select Lyα emitters at $z = 5.7$, our initial sample of line emitters reveals a range of strong line emitters. The peaks in the photometric redshifts are consistent with Hα at $z \sim 0.2$, [OIII] at ~ 0.6, [OII] at $z \sim 1.2$ and Lyα at $z = 5.7$. From our spectroscopic redshift, we find a total of 46 Lyα emitters at $z = 5.7$.

As expected, our sample is dominated by lower redshift line-emitters, mostly composed by sources up to $z \sim 1.2$. In order to isolate LAEs at $z = 5.7$ from our sample we require additional selection criteria, which we will explore in Section 3.2.

3.2   Selection of LAEs at z = 5.7

In order to select Lyα emitters and remove low redshift interlopers, we use the Lyman break technique and identify the break at rest frame 912 Å, blue-ward of the Lyman limit (although, in practice, at $z = 5.7$, radiation blue-ward of Lyα is almost fully absorbed by the Lyα forest; e.g. Madau 1995). LAEs at $z = 5.7$ should have no strong detection in optical wavelengths below the i band. A weak r band detection is possible if the IGM is relatively transparent (and

there are few Lyα forest lines). To summarise, we apply the following criteria, similar to Ouchi et al. (2008):

$$B > B_{2\sigma} \wedge V > V_{2\sigma} \wedge [r > r_{2\sigma} \vee (r < r_{2\sigma} \wedge r - i > 1.0)] \quad (4)$$

where B, V, r and i are the $2''$ magnitudes in the respective bands and the $_{2\sigma}$ subscript indicates the 2σ depth for the images of the respective bands (see Table 2). As there are no available BV data over the full SA22, we apply a small variation of Equation 4 where use ug instead:

$$u > u_{2\sigma} \wedge g > g_{2\sigma} \wedge [r > r_{2\sigma} \vee (r < r_{2\sigma} \wedge r - i > 1.0)] \quad (5)$$

where u, g are the $2''$ magnitudes in the respective bands. This criteria ensures we select sources with no detection in the $BVug$ bands but can have some detection in r as long as there is a strong $i - r$ color break.

In extreme cases, $z \sim 1$ line emitters with a strong Balmer-break could mimic the Lyman-break that we detect. Fortunately, those sources can be identified by their red colors. Similar to Matthee et al. (2015) we reject sources which have significant red colors in the observed NIR bands. Thus, we consider sources with $J - K > 0.5$ to be interlopers. This additional NIR criterion is most important in SA22, where the optical data are relatively shallow.

In order to ensure that our candidates are real detections and not spurious sources, we visually inspect each one of the remaining candidates. We first inspect sources in the narrow band images and reject any fake detections (usually originated by e.g. diffraction patterns from bright sources which were not completely masked). We also visually check that each source does not have an optical detection blueward of the Lyman-break. To do so, we create an optical stack using the available optical bands for each field (BVg for COSMOS, BV for UDS and ug for SA22), which significantly increases the depth of our images.

To summarise, we select line-emitters as Lyα at $z = 5.7$ if:

• They have no optical detection blue-ward of the Lyman-break (Equation 4 or 5).
• They satisfy $J - K < 0.5$, if detected in the NIR.
• They pass visual inspection, which includes both reality of NB excess (and checking for variability and/or moving sources) and no detection in optical bands.

3.3 Comparison with other samples of Lyα emitters at $z = 5.7$

We compare our sample of LAEs with the spectroscopically confirmed sources at $z = 5.7$ provided by Ouchi et al. (2008) (UDS), Hu et al. (2010) (SA22-deep) and Mallery et al. (2012) (COSMOS). We find that we recover 46 spectroscopically confirmed sources from previous studies which are above our conservative Σ detection threshold (other studies typically only apply an EW cut) and that are not in our conservative masked regions.

3.4 Final sample of Lyα emitters at $z = 5.7$

Across the COSMOS, UDS and SA22 fields we identify a total of 514 $z = 5.7$ LAE candidates (currently 46 are spectroscopically confirmed), spanning a range of Lyα luminosities of $10^{42.5} - 10^{44} \, \mathrm{erg \, s^{-1}}$. We will explore the properties

Table 3. Number of candidates after each selection step. The visual inspections step includes individually checking each source first in both the narrow band NB816 and the broad band i images and then for no detection in the deep optical stacks (BV for UDS, BVg for COSMOS and ug for SA22). Note that due to the shallower broad band data in SA22, a large amount of sources passed the initial filtering, but are rejected with the much deeper ug stacks and our visual checks.

COSMOS	# sources
$\Sigma > 3$, $\mathrm{EW_0} > 25\,\text{Å}$	2576
No optical detection	396
After visual inspections	192
UDS	
$\Sigma > 3$, $\mathrm{EW_0} > 25$	981
No optical detection	239
After visual inspections	178
SA22-wide	
$\Sigma > 3$, $\mathrm{EW_0} > 25$	4692
No optical detection	1264
After visual inspections	56
SA22-deep	
$\Sigma > 3$, $\mathrm{EW_0} > 25$	2803
No optical detection	541
After visual inspections	88
Total Lyα z = 5.7 ($\mathbf{z_{spec}}$ confirmed)	514 (46)

of these sources in the following sections. Table 3 shows a summary of the number of sources after each selection criterion. The spatial distribution of the LAEs in all fields can be seen in Figure 2.

4 COMPUTING THE LYα LF

4.1 Completeness correction

Faint sources and sources with weak emission lines may be missed by our selection criteria, causing the measured number density of sources to be underestimated. To estimate the line-flux completeness we follow Sobral et al. (2013), adapted for Lyα studies by Matthee et al. (2015): we construct a sample of high-redshift non line-emitters selected through a simple color break selection ($r - i > 1.5$) and add non-emitters with photometric or spectroscopic redshift higher than 4. Using these sources, in steps of increasing line-flux, we artificially increase their NB816 and i band fluxes and then apply our selection criteria on these simulated sources. By determining the fraction that we retrieve as a function of added line-flux, we obtain a completeness estimation for each luminosity bin, which we apply to each bin in our LF. A higher completeness correction is measured for the fainter sources as they are much easier to be missed. The line-flux completeness per luminosity bin for each field is presented in Table A1. The completeness corrected number counts in the different observed fields as a function of their Lyα luminosity are shown in Figure 5 and in Table A3.

4.2   Filter profile correction

The narrow band filter transmission NB816 has a gaussian distribution with a lower transmission in the wings (Figure 1). Sources which have a redshift in the borders of the filter will only be observed at a fraction of their Lyα luminosity (see e.g. Hu et al. 2010). It is necessary to apply a correction factor that compensates the fact that the filter is not top-hat, otherwise, the number densities of bright LAEs will be systematically underestimated. We apply a correction similar to Matthee et al. (2015). We use the Schechter fit from our data to generate the Lyα luminosity of 1 million sources at a random redshift between $z = 5.65$ and $z = 5.75$ (corresponding to the edges of NB816). For each luminosity bin, the correction factor is determined from the detection ratio of these fake sources retrieved with the two different filter profiles. The effect of the filter profile correction of our LF is shown in Figure A1. The correction is higher for the brightest bins as these LAEs will likely be observed at a fraction of their luminosity due to the filter not being top-hat.

4.3   Aperture corrections

Due to instrumental/observational effects (e.g. seeing/PSF) and mostly due to Lyα photons easily scattering within haloes, Lyα flux can be significantly extended (e.g. Momose et al. 2014; Wisotzki et al. 2016; Matthee et al. 2016a; Borisova et al. 2016). The $2''$ apertures we use are $3 - 4\times$ the PSF, and thus for point-like sources we do not expect aperture corrections to be important, but if sources are physically extended, $2''$ apertures may lead to missing flux. We investigate this by comparing the NB816 fluxes measured in $2''$ with those measured with MAG-AUTO and study any necessary correction as a function of observed $2''$ flux. We find little to no dependence up to at least the highest fluxes, and derive a median correction of $+0.02$ in Lyα luminosity, which we apply (see further discussion in Section 5.3).

4.4   Interloper correction

While in COSMOS and UDS the available broad-band data allows to clearly identify and remove interlopers/lower red-shift line emitters, in SA22 this is not necessarily the case, particularly for the sources with the faintest continuum. In order to mitigate this, we use our combined COSMOS and UDS with full information, but study the dataset assuming the depths of broad-band imaging were the same as SA22-deep and SA22-wide. We find that, as expected, the contamination is higher (10% higher) for SA22-like data-sets. We therefore correct all our luminosity bins in SA22 for this expected extra contamination.

4.5   Obtaining a comparison LF at $z = 6.6$

In order to compare our results at $z = 5.7$, we explore the results and sample presented by Matthee et al. (2015) and apply any necessary corrections/modifications to derive a new, updated $z = 6.6$ LF. We use the same methods for completeness and filter profile corrections. We compute the errors per bin by not only taking into account the Poissonian errors, but also by considering systematic errors due to the completeness and filter profile corrections. Furthermore,
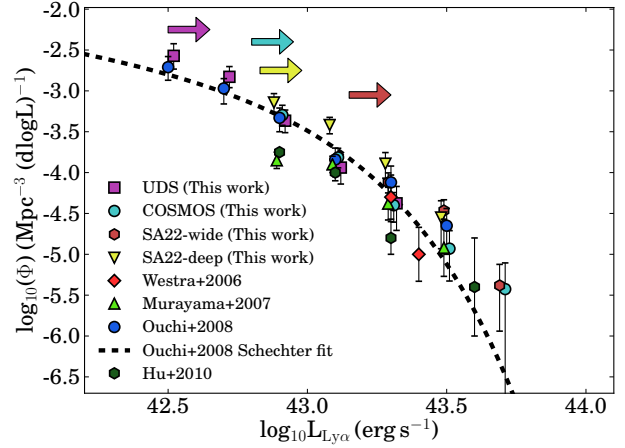

Figure 5. The Lyα luminosity function at $z = 5.7$ based on different fields. For visual reference, a small offset in the luminosities (± 0.02 dex) was used to minimize overlapping of points in the figure. The arrows indicate the luminosity bins for which each field has an average completeness higher than 25%. We find significant field to field variations of ± 0.4 dex in number densities, consistent with results from e.g. Ouchi et al. (2008). We also compare our results per field with previous studies, finding them to be consistent with Murayama et al. (2007) and Ouchi et al. (2008). However, by probing larger, multiple volumes we overcome cosmic variance.

following our selection criteria, we also carefully check for any variable sources and/or moving sources which can contaminate the bright end. Matthee et al. (2015) applied a statistical correction for these potential contaminants, but we chose to investigate sources one by one, following what we do at $z = 5.7$. We note that such statistical correction works very well for COSMOS and UDS, but is a slight underestimation for SA22, as the number of moving sources in SA22 is significantly higher. Nonetheless, we find that none of the results from Matthee et al. (2016a), which are based on spectroscopic follow-up (Sobral et al. 2015), have significantly changed: luminous LAEs ($L_{Ly\alpha} > 10^{43.5}\,\mathrm{erg\,s^{-1}}$) at $z = 6.6$ are more common ($\gtrsim 30$ times) than previously measured by smaller area studies (e.g. Ouchi et al. 2010). We note that we also apply an aperture correction to the $z = 6.6$ LF of $+0.11$, unchanged from Matthee et al. (2015).

5   RESULTS

5.1   The $z = 5.7$ Lyα luminosity function

5.1.1   Field to field variations

We group our LAEs in luminosity bins according to their Lyα luminosity. The observed number density in each bin is corrected for its corresponding line-flux completeness correction. We only include sources from sub-fields with a completeness higher than 25%. The number density for each luminosity bin is calculated by multiplying the number of counts by the completeness factor, divided by the probed volume and bin width. The errors are Poissonian, but we add 30% of the completeness correction in quadrature to obtain the final error per bin.

In Figure 5 we show the $z = 5.7$ Lyα luminosity com-

puted per field. We find that there is significant scatter, of the order of ±0.4 dex in the number densities, at least for the range of luminosities where we can compare results from all our fields. It may well be that such scatter is reduced for fainter sources, but our sample does not allow us to constrain that as we can only investigate that with a single field (UDS) – see Ouchi et al. (2008). Our results per field are also presented in Table A2. Our results highlight the importance of probing multiple fields and caution the over-interpretation of single field "over" or "under" densities, either in the context of reionization or of structure formation.

5.1.2 *Comparison with other z = 5.7 surveys*

Several surveys have published LFs of $z = 5.7$ LAEs, which we compare with our results (see Figure 5). We compare our results with Westra et al. (2006), Murayama et al. (2007) (COSMOS), Ouchi et al. (2008) (UDS) and Hu et al. (2010) (SA22-deep, SSA17, A370 and GOODS-N) in Figure 5. While there are some differences between our selection criteria and the ones applied in these studies, overall we find very good agreement. Moreover, the variance that we see from field to field (see Figure 5) is sufficient to explain any subtle differences between our results per field and those in the literature.

For the COSMOS field, Murayama et al. (2007) applies a much more conservative Σ cut (corresponding to roughly Σ > 5) which leads to missing fainter LAEs. The different Σ cut, together with a different completeness correction (ours is based on line-flux or luminosity, while Murayama et al. 2007 does a correction based on detection completeness) easily explains why our fainter luminosity bin ($\log_{10}L_{Ly\alpha} = 42.9\,\mathrm{erg\,s^{-1}}$) has a higher number density, which fully agrees with our UDS and SA22 estimates, along with those presented in Ouchi et al. (2008).

Within the errors, our results are also fully consistent with those by Ouchi et al. (2008), at all luminosities. Our brightest bin ($\log_{10}L_{Ly\alpha} = 43.7\,\mathrm{erg\,s^{-1}}$) is populated only by our COSMOS and SA22-wide fields, as those have the largest areas (sufficiently large to probe the bright end), but we note that the estimates from COSMOS and SA22-wide fully agree, while we are also in very good agreement with the results from Hu et al. (2010). SA22-deep is both our smallest contiguous field and also the one with the highest number densities (although generally agreeing within the errors with the other fields, particularly given the variance seen). In the SA22-wide field we find number densities consistent with Ouchi et al. (2008) up to $\log_{10}L_{Ly\alpha} = 43.5$ erg s^{-1} and a brighter bin consistent with our COSMOS number density. The bright end of the Lyα LF seems to point towards a deviation from the Schechter fit presented in Ouchi et al. (2008), better explained by a less accentuated exponential drop, or by a single power-law.

5.1.3 *The combined z = 5.7 Lyα luminosity function*

We combine our data from the different fields to obtain a combined Lyα luminosity function at $z = 5.7$. We show the results in Figure 6 and Table A3.

We fit a Schechter function (Schechter 1976), defined by three parameters: the power-law slope α, the characteristic number density $\phi^\star$ and the characteristic luminosity $L^\star$.

Table 4. Parameters for the best Schechter function fits for the Lyα LFs at $z = 5.7$ and $z = 6.6$ (recomputed Matthee et al. 2015). We allow α to vary, but we also fix α to -2.0 and -1.5.

Redshift	α	$\log_{10}L^\star_{Ly\alpha}$ (erg s^{-1})	$\log_{10}\Phi^\star$ (Mpc^{-3})
$z = 5.7$	$-2.3^{+0.4}_{-0.3}$	$43.42^{+0.50}_{-0.22}$	$-4.02^{+0.48}_{-0.93}$
	-1.5 (fix)	$43.06^{+0.05}_{-0.04}$	$-3.25^{+0.09}_{-0.10}$
	-2.0 (fix)	$43.25^{+0.09}_{-0.06}$	$-3.63^{+0.12}_{-0.16}$
$z = 6.6$	$-2.3^{+0.4}_{-0.3}$	$43.45^{+0.35}_{-0.18}$	$-4.48^{+0.43}_{-0.68}$
	-1.5 (fix)	$43.12^{+0.04}_{-0.03}$	$-3.73^{+0.07}_{-0.06}$
	-2.0 (fix)	$43.30^{+0.07}_{-0.05}$	$-4.13^{+0.10}_{-0.10}$

In Table 4, we present best-fit parameters of the Schechter function at $z = 5.7$. We find the faint end slope α to be particularly steep: $\alpha = -2.3^{+0.4}_{-0.3}$. This is in very good agreement with recent results from Dressler et al. (2015) at the same redshift who found α to be $-2.35 < \alpha < -1.95$ (while we find $-2.6 < \alpha < -1.9$, $1\,\sigma$). It is therefore clear that the Lyα luminosity function is very steep just after re-ionisation and may be steeper than the UV luminosity function at the same redshift ($\alpha \approx -1.9$; e.g. Bouwens et al. 2015). Note that such a steep faint-end slope at $z = 5.7$ is already preferred by the fit in Ouchi et al. (2008) and is consistent with theoretical expectations (Gronke et al. 2015).

We also fit our LF by fixing the faint-end slope to $\alpha = -2.0$ and $\alpha = -1.5$ and allow $\Phi^\star$ and $L^\star$ to vary. This allows our results to be directly compared with other studies which fixed α to the same values. The results are presented in Table 4.

5.2 Evolution from z = 5.7 to z ∼ 7 and beyond

In Section 4.5 we discuss the steps we took to obtain a comparable and updated $z = 6.6$ Lyα luminosity function, based on Matthee et al. (2015). We show the recomputed $z = 6.6$ Lyα LF, and a comparison with our $z = 5.7$ measurement in Figure 6. The recomputed $z = 6.6$ LF is fully presented in Table A3.

We find that both $z = 6.6$ and $z = 5.7$ are best fit with a very steep α of ~ -2.3. At a fixed α, our results show a significant decline in the number density of the more "typical"/faint Lyα emitters from $z = 5.7$ to $z = 6.6$, with ϕ^* declining by 0.5 dex. However, and in very good agreement with Matthee et al. (2015), we find little to no evolution at the bright end, with L^* showing no significant evolution, or only a very weak increase of $\sim 0.05 - 0.1$ dex from $z = 5.7 - 6.6$ (depending on α). In practice, our results show that the number density of bright Lyα emitters ($L_{Ly\alpha} > 10^{43.5}\mathrm{erg\,s^{-1}}$) shows no significant evolution from $z = 5.7$ to $z = 6.6$, confirming the results suggested in Matthee et al. (2015). We note that while we discuss the luminosity functions in the context of their Schechter fits, the results presented hold if we fit them with e.g. single or double power-laws. At $z = 6.6$, the spectroscopic confirmation of the sources responsible for these high Lyα luminosities is starting to reveal their uniqueness (e.g. multi-component, very low metallicities, blue Lyα wings, range of sizes, see e.g. Himiko, MASOSA, CR7, COLA1; Ouchi et al. 2013; Sobral et al. 2015; Hu et al. 2016), providing important hints

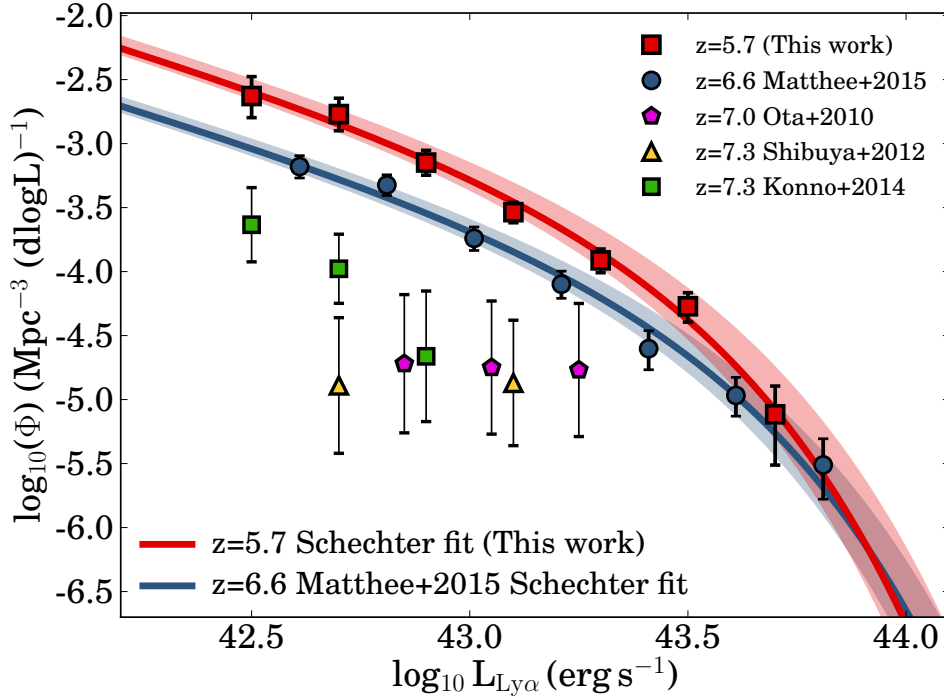**Figure 6.** Evolution of the Lyα LF from $z = 5.7$ to $z = 6.6$. The $z = 6.6$ LF is our updated version from Matthee et al. (2015), see Section 4.5. The colored regions around the best Schechter fit show the 1σ error in L^*. We observe a strong decrease in the number density of the fainter LAEs as we increase with redshift up to $z = 6.6$ and also $z > 7$ (Ota et al. 2010; Shibuya et al. 2012; Konno et al. 2014). This decrease can likely be explained by a more neutral IGM as we go deeper into the reionization epoch. However, there seems to be no evolution for the brighter sources, which can likely be explained by a preferential reionization around the brightest sources. There is currently a lack of comparable surveys at $z > 7$ at the brightest luminosities.

that may explain how these sources have been able to likely reionize their surroundings already at $z \sim 7$. Further observations will be able to confirm a larger, statistical sample at $z \sim 7$, but our new sample at $z = 5.7$ is uniquely suited to be directly compared.

Figure 6 also presents results from several $z > 7$ narrow band surveys from the literature, which we compare with $z = 6.6$ and $z = 5.7$. The trend that we see from $z = 5.7$ to $z = 6.6$ of significant decrease in the number density of faint Lyα emitters seems to continue at a fast pace to $z \sim 7$ and beyond (Ota et al. 2010; Shibuya et al. 2012; Konno et al. 2014). We provide a more detailed discussion about the differential evolution of the Lyα as an imprint of reionization in Section 6. There is currently a lack of comparable surveys at $z > 7$ at the brightest luminosities, so it is not yet possible to test whether the lack of evolution at the bright end still holds at $z > 7$.

5.3   The Lyα sizes and evolution at $z = 5.7 - 6.6$

Since the Lyα transition is resonant, Lyα photons scatter in a medium with neutral hydrogen. Because of this, Lyα photons tend to escape over much large radii than their UV and Hα counterparts, making them observable as Lyα haloes (e.g. Rauch et al. 2008; Steidel et al. 2011; Momose et al. 2014; Matthee et al. 2016a). Therefore, the aperture that is used to measure Lyα is critical (e.g. Wisotzki et al. 2016). Typically, LAE surveys have attempted to take extended

Lyα emission into account by using MAG-AUTO measurements (e.g. Ouchi et al. 2010; Konno et al. 2016) or relatively large apertures (e.g. Murayama et al. 2007; Hu et al. 2010, who use 3″ apertures at $z = 5.7$). However, the total measured magnitude with MAG-AUTO depends on the depth of the narrow-band imaging, such that a comparison between surveys and redshifts is challenging, particularly as Wisotzki et al. (2016) show that Lyα extends well beyond the typical limiting surface brightness of narrow-band surveys.

While we use fixed 2″ apertures in similar excellent seeing conditions at both $z = 5.7$ and $z = 6.6$ (as this allows to understand the completeness and selection function in an optimal way; c.f. Matthee et al. 2015), we correct for any flux missed as described in Section 4.3.

Matthee et al. (2015) found that 2″ apertures systematically underestimate Lyα luminosities at $z = 6.6$ (compared to the MAG-AUTO) with a median offset of 0.11 dex over the spectroscopically confirmed sample of LAEs (confirmed in Ouchi et al. 2010). Here we extend this analysis to the full sample of sources at both $z = 5.7$ and $z = 6.6$. We find that the median offset between the MAG-AUTO luminosity and the 2″ aperture offset at $z = 6.6$ is 0.11 dex, while it is only 0.02 dex at $z = 5.7$; see Figure 7. The latter explains why our 2″ measurements result in very similar number densities as literature studies with larger apertures at $z = 5.7$, see Fig. 5.

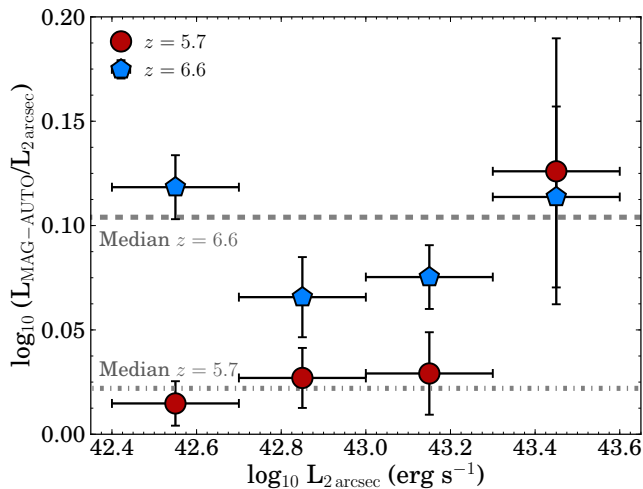By splitting the sample of LAEs in bins of Lyα luminosity (in 2″ apertures), we find that at $z = 5.7$ the offset in-

Figure 7. The median difference in MAG-AUTO luminosity and luminosity within 2″ apertures in bins of the 2″ aperture Lyα luminosity for LAE samples at $z = 5.7$ and $z = 6.6$. The dashed and dashed-dotted grey lines indicate the median of all LAEs in the sample, which is obviously dominated by low luminosity sources. At both redshifts, more centrally luminous LAEs also have relatively more flux at larger radii (which is captured by MAG-AUTO). At faint central luminosities LAEs at $z = 6.6$ appear more extended, which could be due to increased scattering in HI around galaxies. We note that this may be one of the causes for the apparent evolution in the Lyα LF, and may also be important to consider when interpreting the spectroscopic follow-up of UV-selected galaxies with low Lyα luminosities, as slits will recover even less of the total flux.

creases slightly with increasing Lyα luminosity (see Fig. 7). Specifically, the most luminous LAEs have larger Lyα haloes (and more flux at larger radii) than the typical fainter ones. Interestingly, we find a different behaviour at $z = 6.6$. While the brightest $z = 6.6$ Lyα seem to be as extended as those at $z = 5.7$ (these are the ones that may have already been able to fully ionise the surrounding environment), fainter Lyα emitters at $z = 6.6$ are all more extended than comparable sources at $z = 5.7$. Together with the differential evolution of the Lyα LF, our results provide strong evidence for reionization effects being much stronger for the faint sources than for the bright ones. We discuss this trend further in Section 6.

A similar but more careful analysis of the extent of Lyα emission at $z = 5.7 − 6.6$ than our own has been done by Momose et al. (2014), who created stacked narrow band and broad band images of the LAEs in UDS from Ouchi et al. (2008, 2010). They observed that Lyα is extended, being more extended than their UV counterpart (while also being more extended than the PSF of their images; a similar trend is found for individual LAEs by e.g. Wisotzki et al. 2016). Momose et al. 2014 found evidence of an increase in the scale length of Lyα from $z = 5.7$ to $z = 6.6$. However, they did not separate their sample in bins of luminosity and their results are obtained with median stacking. This means that the faintest sources dominate (as there are more faint sources than luminous ones) and that these results are more representative of a "typical" LAE, with $L_{Lyα} \sim 10^{42.6}\,\mathrm{erg\,s^{-1}}$.

The median evolution in the scale length of Lyα haloes from LAEs estimated in Momose et al. (2014) is thus consistent with the difference between MAG-AUTO and 2″ measurements that we find for relatively faint LAEs between $z = 5.7$ and $z = 6.6$.

6 DISCUSSION: IMPRINTS FROM REIONIZATION?

As noted before, the observed Lyα luminosity at a fixed spatial scale is expected to decrease in the reionization era, as an increasingly neutral IGM scatters Lyα photons into larger, extended haloes (e.g. Dijkstra 2014). Our results are consistent with witnessing such predictions directly. Here we discuss the differences we observe in the Lyα luminosity function between $z = 5.7$ and $z = 6.6$, and also our results on the extent of Lyα emitters at $z = 5.7$ and $z = 6.6$. For earlier work, see e.g. Dijkstra et al. (2007), Ouchi et al. (2010) and Hu et al. (2010).

We observe strong differential evolution of the Lyα LF from $z \sim 6$ to $z \sim 7$, with a significant decrease ($−0.5\,\mathrm{dex}$) in the number density for Lyα luminosities below L^*. The drop in the observability of faint LAEs may well be explained by a larger fraction of neutral IGM at $z > 6$ caused by reionization not being completed. The brightest emitters would not suffer from such a decline because their strong Lyα emission is easier to be observed, as previously illustrated by the simple toy model in Matthee et al. (2015). This model assumes that the Lyα luminosity scales with the ionising output and LAEs are only observed if they are either capable of ionising the IGM around them, or are strongly clustered. To first order, a stronger ionising output for brighter LAEs is expected because Lyα is a recombination line (such that at fixed escape fraction, a higher Lyα luminosity scales with the number of ionising photons). Also, as shown in Matthee et al. (2016b), LAEs at $z = 2.2$ typically produce more ionising photons per unit UV luminosity than more typical galaxies such as Hα emitters (HAEs). Furthermore, as hypothesised by Dijkstra & Gronke (2016), ISM conditions which favor the escape of Lyα photons also likely favor the escape of Lyman continuum (LyC) photons (for example due to a porous ISM), such that in addition to producing more ionising photons, LAEs could also leak more ionising photons into the IGM.

Recent evidence from Stark et al. (2016) shows that the fraction of bright UV selected galaxies (LBGs) with strong Lyα emission is much higher than was previously found (e.g. Schenker et al. 2014; Pentericci et al. 2014; Schmidt et al. 2016) when they are selected on strong nebular lines (e.g. Hβ/[OIII]). This is likely because UV-bright galaxies are in over-dense regions and emit copious amount of ionising radiation (inferred from observed high ionization UV lines as CIII] and their high EW optical nebular lines). Such conditions may also favor the production of Lyα photons and lead to larger ionised bubbles. Therefore, these observations are in principle consistent with the observed evolution of the Lyα LF, where we observe reionization completing first around luminous LAEs.

A unique benefit of narrow-band Lyα observations over (slit) spectroscopy is that narrow-band imaging gives information on the spatial extent of Lyα emission, which could

be connected to the neutral fraction of the IGM (e.g. Dijkstra & Loeb 2008). As we show in Figure 7, we find that the median difference between $2''$ apertures and the total magnitude (as observed with MAG-AUTO) is much smaller at $z = 5.7$ than at $z = 6.6$. Most interestingly, the major difference is found at the faintest luminosities. At $z = 6.6$, LAEs which have a low central luminosity have a relatively much larger total luminosity than at $z = 5.7$. This means that at a fixed surface brightness limit (note that the limiting surface brightness at $z = 6.6$ is actually even slightly higher), faint LAEs are more extended at $z = 6.6$ than at $z = 5.7$. For more luminous LAEs the difference is much smaller. This effect can easily be explained in the framework of the Matthee et al. (2015) toy-model: faint LAEs are surrounded by a relatively more neutral IGM, such that there is more resonant scattering leading to more extended emission.

The evolution of the Lyα LF and the extent of Lyα for different luminosities may very well be explained by a patchy reionization scenario where the IGM is ionised first around luminous LAEs. However, internal effects from galaxies may also be important. Furthermore, studying the clustering of both bright and faint LAEs and how it evolves from e.g. $z = 5.7$ to $z = 6.6$ and beyond (e.g. Mesinger 2010; Ouchi et al. 2010) will provide the extra, necessary constraints. A similar analysis with future larger samples of LAEs (for example from the Hyper Suprime Cam survey) will be very useful to confirm the observed trends.

Our results also mean that a careful approach is required in order to interpret the observed Lyα fraction for samples of LBGs at different redshifts in terms of a varying neutral fraction due to reionization, because different samples of LBGs show very different Lyα fractions. Curtis-Lake et al. (2012) found a remarkably high fraction of strong LAEs amongst luminous LBGs, Stark et al. (2016) found a higher Lyα fraction for LBGs selected on strong nebular emission and Erb et al. (2016) found that $z \sim 2$ galaxies with extreme line ratios have high Lyα fractions. Moreover, our results show that typical, faint Lyα emitters become more extended as we go into the reionization epoch, with the same (or even less) flux being spread over larger areas. This is an additional challenge for the traditional slit spectroscopy follow-up, which will struggle to detect any Lyα if the flux is significantly extended.

7 CONCLUSIONS

We have constructed the largest Lyα narrow band survey at $z = 5.7$, when re-ionization is close to complete. We have surveyed a total area of $7\,\mathrm{deg}^2$ and a volume of $6.3 \times 10^6\,\mathrm{Mpc}^3$ at $z = 5.7$, covering the COSMOS, UDS and SA22 fields. Here we summarize the main conclusions:

• By identifying strong line-emitters with a Lyman break, we find 514 LAE candidates at $z = 5.7$ with $\mathrm{EW}_0 > 25$ Å ($\mathrm{EW}_0 \sim 25 - 1000$ Å) and luminosities ranging from $10^{42.5} - 10^{44}\,\mathrm{erg\,s}^{-1}$, in a single, homogeneous data-set.

• We find that cosmic variance plays a major role, with variations of $\pm 0.4\,\mathrm{dex}$ in number densities of Lyα emitters from field to field.

• By combining all our fields and overcoming cosmic variance, we find that the faint end slope of the $z = 5.7$ Lyα luminosity function is very steep, with $\alpha = -2.3^{+0.4}_{-0.3}$. If

we fix $\alpha = -2.0$, we find $L^\star = 10^{43.22^{+0.08}_{-0.05}}\,\mathrm{erg\,s}^{-1}$ and $\Phi^\star = -3.60^{+0.12}_{-0.16}\,\mathrm{Mpc}^{-3}$.

• We also present an updated $z = 6.6$ Lyα luminosity function, based on comparable volumes, and obtained with the same methods, which we directly compare with that at $z = 5.7$.

• We find significant evolution from $z = 5.7$ (after re-ionization) to $z = 6.6$ (within the epoch of re-ionization) at the faint end. We find that the fainter the luminosity, the stronger the drop in the number density of Lyα emitters. The strong decrease of the number density of faint Lyα emitters continues to $z \sim 7$.

• At bright Lyα luminosities ($\mathrm{L}_{\mathrm{Ly}\alpha} > 10^{43.5}\,\mathrm{erg\,s}^{-1}$) we find no evolution in the number density of Lyα emitters when we enter the re-ionization era. This is consistent with bright Lyα emitters being preferentially observable because they already are in ionized bubbles even at $z \sim 7$.

• Faint Lyα emitters at $z = 6.6$ show more extended haloes than those at $z = 5.7$, suggesting that neutral Hydrogen plays a more important role of scattering Lyα photons at $z = 6.6$.

All together, our results indicate that we are observing patchy reionization happening first around the brightest Lyα emitters, allowing the number densities of those sources to remain unaffected by the increase of neutral Hydrogen from $z \sim 5$ to $z \sim 7$. We observe a preferential evolution of the faint end of the Lyα LF from $z = 5.7$ to $z = 6.6$. There is a decrease in the faint end while the bright end shows little to no evolution. We also observe no evolution in the sizes of the brighter emitters, which could be interpreted as showing no evidence of extra scattering around them from $z = 5.7$ to $z = 6.6$, while faint sources show a significant difference, presenting much more flux at larger radii, which could be explained by faint LAEs being located in a more neutral IGM leading to more resonant scattering and extended emission. The spectroscopic confirmation of relatively bright Lyα emitters beyond $z \sim 7$ and approaching $z \sim 9$ (Oesch et al. 2015; Zitrin et al. 2015) may already be hinting that our results may hold to even higher redshifts.

The nature and diversity of bright Lyα sources at $z = 6.6$, which we find to have essentially the same number density as those at $z = 5.7$, are starting to be unveiled. Spectroscopic follow up (e.g. Ouchi et al. 2013; Sobral et al. 2015; Zabl et al. 2015; Hu et al. 2016), detailed modelling (e.g. Hartwig et al. 2015; Dijkstra et al. 2016; Agarwal et al. 2016; Visbal et al. 2016; Smidt et al. 2016; Smith et al. 2016) and other observations with HST and ALMA (Ouchi et al. 2013; Sobral et al. 2015; Schaerer et al. 2015; Bowler et al. 2016) are revealing a surprising diversity. Current results indicate that these sources may have a range of powering sources (from metal poor populations to multiple stellar populations and also AGN, including potentially direct collapse black holes). Regardless of their nature, their observability requires the production and emission of the necessary amount of ionising LyC photons capable of ionising a large enough local bubble to make them observable as bright Lyα sources already at $z = 6.6$. Thus, even though these sources are not as abundant as the more typical, faint sources, they may well play an important role in cosmic reionization, at least at very early stages, a scenario which would be in agreement with what is seen by Matthee et al. (2016b). Further

observations of our sample of bright $z = 5.7$ sources and of much larger, statistical samples at $z \sim 5 - 7$ will certainly shed light over many of the current open questions, while the availability of JWST will provide a revolutionary window into the physical conditions within these sources.

REFERENCES

Adams J. J., et al., 2011, ApJS, 192, 5
Agarwal B., Johnson J. L., Zackrisson E., Labbe I., van den Bosch F. C., Natarajan P., Khochfar S., 2016, MNRAS,
Astropy Collaboration et al., 2013, A&A, 558, A33
Bacon R., et al., 2015, AAP, 575, A75

Bayliss M. B., Wuyts E., Sharon K., Gladders M. D., Hennawi J. F., Koester B. P., Dahle H., 2010, ApJ, 720, 1559
Becker G. D., Bolton J. S., Madau P., Pettini M., Ryan-Weber E. V., Venemans B. P., 2015, MNRAS, 447, 3402
Bertin E., 2006, in Gabriel C., Arviset C., Ponz D., Enrique S., eds, Astronomical Society of the Pacific Conference Series Vol. 351, Astronomical Data Analysis Software and Systems XV. p. 112
Bertin E., Arnouts S., 1996, AAPS, 117, 393
Bertin E., Mellier Y., Radovich M., Missonnier G., Didelon P., Morin B., 2002, in Bohlender D. A., Durand D., Handley T. H., eds, Astronomical Society of the Pacific Conference Series Vol. 281, Astronomical Data Analysis Software and Systems XI. p. 228
Blanc G. A., et al., 2011, ApJ, 736, 31
Borisova E., et al., 2016, preprint, (arXiv:1605.01422)
Boulade O., et al., 2003, in Iye M., Moorwood A. F. M., eds, Proc. SPIEVol. 4841, Instrument Design and Performance for Optical/Infrared Ground-based Telescopes. pp 72–81, doi:10.1117/12.459890
Bouwens R. J., et al., 2015, ApJ, 803, 34
Bowler R. A. A., Dunlop J. S., McLure R. J., McLeod D. J., 2016, preprint, (arXiv:1605.05325)
Bunker A. J., Warren S. J., Hewett P. C., Clements D. L., 1995, MNRAS, 273, 513
Capak P., et al., 2007, ApJS, 172, 99
Capak P. L., et al., 2015, Nature, 522, 455
Caruana J., Bunker A. J., Wilkins S. M., Stanway E. R., Lacy M., Jarvis M. J., Lorenzoni S., Hickey S., 2012, MNRAS, 427, 3055
Caruana J., Bunker A. J., Wilkins S. M., Stanway E. R., Lorenzoni S., Jarvis M. J., Ebert H., 2014, MNRAS, 443, 2831
Casali M., et al., 2007, A&A, 467, 777
Cassata P., et al., 2011, A&A, 525, A143
Cassata P., et al., 2015, A&A, 573, A24
Castellano M., et al., 2016, ApJ, 818, L3
Cirasuolo M., et al., 2007, MNRAS, 380, 585
Cowie L. L., Hu E. M., 1998, AJ, 115, 1319
Curtis-Lake E., et al., 2012, MNRAS, 422, 1425
Dijkstra M., 2014, Publ. Astron. Soc. Australia, 31, e040
Dijkstra M., Gronke M., 2016, preprint, (arXiv:1604.08208)
Dijkstra M., Loeb A., 2008, MNRAS, 386, 492
Dijkstra M., Lidz A., Wyithe J. S. B., 2007, MNRAS, 377, 1175
Dijkstra M., Gronke M., Sobral D., 2016, ApJ, 823, 74
Dressler A., Henry A., Martin C. L., Sawicki M., McCarthy P., Villaneuva E., 2015, ApJ, 806, 19
Dunlop J. S., McLure R. J., Robertson B. E., Ellis R. S., Stark D. P., Cirasuolo M., de Ravel L., 2012, MNRAS, 420, 901
Dunlop J. S., et al., 2016, preprint, (arXiv:1606.00227)
Erb D. K., Pettini M., Steidel C. C., Strom A. L., Rudie G. C., Trainor R. F., Shapley A. E., Reddy N. A., 2016, preprint, (arXiv:1605.04919)
Fan X., et al., 2006, ApJ, 132, 117
Finkelstein S. L., et al., 2015, ApJ, 810, 71
Fontana A., et al., 2010, ApJ, 725, L205
Furusawa H., et al., 2008, ApJS, 176, 1
Gronke M., Dijkstra M., Trenti M., Wyithe S., 2015, MNRAS, 449, 1284
Hartwig T., et al., 2015, preprint, (arXiv:1512.01111)
Hayes M., Schaerer D., Östlin G., 2010, AAP, 509, L5
Hayes M., Schaerer D., Östlin G., Mas-Hesse J. M., Atek H., Kunth D., 2011, ApJ, 730, 8
Hu E. M., Cowie L. L., Barger A. J., Capak P., Kakazu Y., Trouille L., 2010, ApJ, 725, 394
Hu E. M., Cowie L. L., Songaila A., Barger A. J., Rosenwasser B., Wold I., 2016, preprint, (arXiv:1606.03526)
Iye M., et al., 2006, Nature, 443, 186
Karman W., et al., 2015, AAP, 574, A11

Kashikawa N., et al., 2011, ApJ, 734, 119

Khostovan A. A., Sobral D., Mobasher B., Best P. N., Smail I., Stott J. P., Hemmati S., Nayyeri H., 2015, MNRAS, 452, 3948

Khostovan A. A., Sobral D., Mobasher B., Smail I., Darvish B., Nayyeri H., Hemmati S., Stott J. P., 2016, preprint, (arXiv:1604.02456)

Kim J.-W., Im M., Lee S.-K., Edge A. C., Wake D. A., Merson A. I., Jeon Y., 2015, ApJ, 806, 189

Konno A., et al., 2014, ApJ, 797, 16

Konno A., Ouchi M., Nakajima K., Duval F., Kusakabe H., Ono Y., Shimasaku K., 2016, ApJ, 823, 20

Laigle C., et al., 2016, preprint, (arXiv:1604.02350)

Lawrence A., et al., 2007, MNRAS, 379, 1599

Ly C., et al., 2007, ApJ, 657, 738

Ly C., Lee J. C., Dale D. A., Momcheva I., Salim S., Staudaher S., Moore C. A., Finn R., 2011, ApJ, 726, 109

Madau P., 1995, ApJ, 441, 18

Madau P., Dickinson M., 2014, ARAA, 52, 415

Maiolino R., et al., 2015, MNRAS, 452, 54

Malhotra S., Rhoads J. E., 2004, ApJL, 617, L5

Mallery R. P., et al., 2012, ApJ, 760, 128

Martin C. L., Sawicki M., 2004, ApJ, 603, 414

Matthee J. J. A., et al., 2014, MNRAS, 440, 2375

Matthee J., Sobral D., Santos S., Röttgering H., Darvish B., Mobasher B., 2015, MNRAS, 451, 400

Matthee J., Sobral D., Oteo I., Best P., Smail I., Röttgering H., Paulino-Afonso A., 2016a, MNRAS,

Matthee J., Sobral D., Best P., Khostovan A. A., Oteo I., Bouwens R., Röttgering H., 2016b, preprint, (arXiv:1605.08782)

McCracken H. J., et al., 2012, A&A, 544, A156

Mesinger A., 2010, MNRAS, 407, 1328

Miyazaki S., et al., 2002, PASJ, 54, 833

Momose R., et al., 2014, MNRAS, 442, 110

Murayama T., et al., 2007, ApJs, 172, 523

Nilsson K. K., et al., 2007, A&A, 471, 71

Oesch P. A., et al., 2015, ApJ, 804, L30

Ono Y., et al., 2012, ApJ, 744, 83

Ota K., et al., 2010, ApJ, 722, 803

Ouchi M., et al., 2004, ApJ, 611, 660

Ouchi M., et al., 2008, ApJs, 176, 301

Ouchi M., et al., 2010, ApJ, 723, 869

Ouchi M., et al., 2013, ApJ, 778, 102

Partridge R. B., Peebles P. J. E., 1967, ApJ, 147, 868

Pentericci L., et al., 2014, ApJ, 793, 113

Pritchet C. J., 1994, PASP, 106, 1052

Rauch M., et al., 2008, ApJ, 681, 856

Rhoads J. E., Malhotra S., Dey A., Stern D., Spinrad H., Jannuzi B. T., 2000, ApJL, 545, L85

Rhoads J. E., et al., 2003, AJ, 125, 1006

Robertson B. E., Ellis R. S., Dunlop J. S., McLure R. J., Stark D. P., 2010, Nature, 468, 49

Sawicki M., et al., 2008, ApJ, 687, 884

Schaerer D., Boone F., Zamojski M., Staguhn J., Dessauges-Zavadsky M., Finkelstein S., Combes F., 2015, A&A, 574, A19

Schechter P., 1976, ApJ, 203, 297

Schenker M. A., Stark D. P., Ellis R. S., Robertson B. E., Dunlop J. S., McLure R. J., Kneib J.-P., Richard J., 2012, ApJ, 744, 179

Schenker M. A., Ellis R. S., Konidaris N. P., Stark D. P., 2014, ApJ, 795, 20

Schmidt K. B., et al., 2016, ApJ, 818, 38

Shibuya T., Kashikawa N., Ota K., Iye M., Ouchi M., Furusawa H., Shimasaku K., Hattori T., 2012, ApJ, 752, 114

Shimasaku K., et al., 2006, PASJ, 58, 313

Skrutskie M. F., et al., 2006, AJ, 131, 1163

Smidt J., Wiggins B. K., Johnson J. L., 2016, preprint, (arXiv:1603.00888)

Smith A., Bromm V., Loeb A., 2016, preprint, (arXiv:1602.07639)

Sobral D., et al., 2009, MNRAS, 398, L68

Sobral D., Smail I., Best P. N., Geach J. E., Matsuda Y., Stott J. P., Cirasuolo M., Kurk J., 2013, MNRAS, 428, 1128

Sobral D., Matthee J., Darvish B., Schaerer D., Mobasher B., Röttgering H. J. A., Santos S., Hemmati S., 2015, ApJ, 808, 139

Stark D. P., Ellis R. S., Richard J., Kneib J.-P., Smith G. P., Santos M. R., 2007, ApJj, 663, 10

Stark D. P., Ellis R. S., Chiu K., Ouchi M., Bunker A., 2010, MNRAS, 408, 1628

Stark D. P., et al., 2016, preprint, (arXiv:1606.01304)

Steidel C. C., Bogosavljević M., Shapley A. E., Kollmeier J. A., Reddy N. A., Erb D. K., Pettini M., 2011, ApJ, 736, 160

Taniguchi Y., et al., 2005, PASJ, 57, 165

Taniguchi Y., et al., 2007, ApJS, 172, 9

Taylor M. B., 2006, in Gabriel C., Arviset C., Ponz D., Enrique S., eds, Astronomical Society of the Pacific Conference Series Vol. 351, Astronomical Data Analysis Software and Systems XV. p. 666

Visbal E., Haiman Z., Bryan G. L., 2016, MNRAS,

Warren S. J., et al., 2007, arXiv:0703037,

Watson D., Christensen L., Knudsen K. K., Richard J., Gallazzi A., Michałowski M. J., 2015, Nature, 519, 327

Westra E., et al., 2006, AAP, 455, 61

Wisotzki L., et al., 2016, A&A, 587, A98

Zabl J., Nørgaard-Nielsen H. U., Fynbo J. P. U., Laursen P., Ouchi M., Kjærgaard P., 2015, MNRAS, 451, 2050

Zitrin A., et al., 2015, ApJ, 810, L12

van Breukelen C., Jarvis M. J., Venemans B. P., 2005, MNRAS, 359, 895

APPENDIX A: FILTER PROFILE CORRECTIONS AND LFS

Figure A1 shows the effect of our filter profile corrections. We show the completeness corrected number densities of LAEs in bins of Lyα luminosity for individual fields at $z = 5.7$ (Table A2) and for the combined coverage at $z = 5.7$ and $z = 6.6$ (Table A3).

This paper has been typeset from a TeX/LaTeX file prepared by the author.

Table A1. For each field we present the median line-flux completeness per bin, which we use to correct the $z = 5.7$ number densities. We only consider number densities from sub-fields with a line-flux completeness higher than 25%.

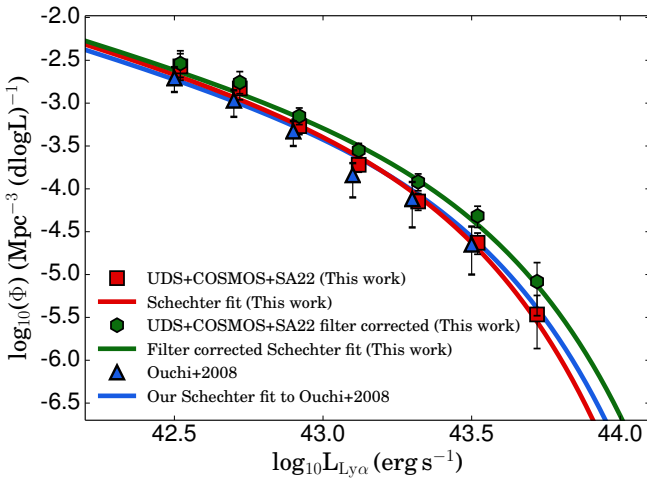| Luminosity bins	Line-flux completeness			
$\log_{10}$L [erg s^{-1}]	Percentage [%]			
	(UDS)	(COSMOS)	(SA22-deep)	(SA22-wide)
42.5 ± 0.1	27	< 25	< 25	< 25
42.7 ± 0.1	30	< 25	< 25	< 25
42.9 ± 0.1	45	37	36	< 25
43.1 ± 0.1	53	54	56	< 25
43.3 ± 0.1	61	65	68	51
43.5 ± 0.1	73	73	77	63
43.7 ± 0.1	83	80	84	74

Figure A1. The number densities in luminosity bins from our survey in the UDS, COSMOS and SA22 fields (red squares) and the bins from Ouchi et al. (2008) in blue triangles. A small luminosity correction of +0.02 was applied to our luminosity bins to correct for extended emission (this correction is discussed in §5.3). The Schechter fits to the luminosity bins from our study agrees very well with Ouchi et al. (2008). In green we also show the luminosity bins from this work after we apply a filter profile bias correction (we estimate this correction in §4.2) and the corrected LF Schechter fit. The effect of this correction is strongest at the brightest bins.

Table A2. The completeness corrected number density of LAEs in the different surveyed fields at $z = 5.7$.

Field	Luminosity bin $\log_{10}$L [erg s^{-1}]	Number density $\log_{10}\Phi/\mathrm{dlogL}$ [Mpc^{-3}]
UDS	42.5 ± 0.1	$-2.57^{+0.15}_{-0.16}$
	42.7 ± 0.1	$-2.82^{+0.13}_{-0.13}$
	42.9 ± 0.1	$-3.37^{+0.13}_{-0.15}$
	43.1 ± 0.1	$-3.94^{+0.16}_{-0.20}$
	43.3 ± 0.1	$-4.37^{+0.21}_{-0.33}$
COSMOS	42.9 ± 0.1	$-3.30^{+0.12}_{-0.13}$
	43.1 ± 0.1	$-3.81^{+0.11}_{-0.13}$
	43.3 ± 0.1	$-4.40^{+0.16}_{-0.21}$
	43.5 ± 0.1	$-4.93^{+0.22}_{-0.39}$
	43.7 ± 0.1	$-5.42^{+0.32}_{-\infty}$
SA22-deep	42.9 ± 0.1	$-3.09^{+0.11}_{-0.12}$
	43.1 ± 0.1	$-3.37^{+0.09}_{-0.11}$
	43.3 ± 0.1	$-3.84^{+0.14}_{-0.18}$
	43.5 ± 0.1	$-4.50^{+0.21}_{-0.38}$
SA22-wide	43.3 ± 0.1	$-4.07^{+0.11}_{-0.13}$
	43.5 ± 0.1	$-4.41^{+0.13}_{-0.16}$
	43.7 ± 0.1	$-5.33^{+0.26}_{-0.56}$

Table A3. The completeness and filter profile bias corrected luminosity functions at $z = 5.7$ and $z = 6.6$ from this study. Note that we corrected the bins for extended emission (see Section 5.3).

Redshift	Luminosity bin $\log_{10}L$ [erg s^{-1}]	Volume [10^6 Mpc^3]	Observed number density $\log_{10}\Phi/d\log L$ [Mpc^{-3}]	Corrected number density $\log_{10}\Phi/d\log L$ [Mpc^{-3}]
$z = 5.7$	42.52 ± 0.1	0.19	$-3.16^{+0.08}_{-0.09}$	$-2.63^{+0.16}_{-0.17}$
	42.72 ± 0.1	0.65	$-3.32^{+0.05}_{-0.06}$	$-2.77^{+0.12}_{-0.13}$
	42.92 ± 0.1	3.09	$-3.65^{+0.04}_{-0.04}$	$-3.15^{+0.10}_{-0.10}$
	43.12 ± 0.1	3.09	$-3.89^{+0.05}_{-0.05}$	$-3.54^{+0.08}_{-0.08}$
	43.32 ± 0.1	6.30	$-4.34^{+0.05}_{-0.06}$	$-3.91^{+0.09}_{-0.10}$
	43.52 ± 0.1	6.30	$-4.70^{+0.08}_{-0.10}$	$-4.27^{+0.11}_{-0.12}$
	43.72 ± 0.1	6.30	$-5.62^{+0.20}_{-0.37}$	$-5.12^{+0.22}_{-0.40}$
$z = 6.6$	42.61 ± 0.1	0.38	$-3.46^{+0.09}_{-0.08}$	$-3.18^{+0.08}_{-0.09}$
	42.81 ± 0.1	0.64	$-3.59^{+0.08}_{-0.07}$	$-3.32^{+0.08}_{-0.08}$
	43.01 ± 0.1	1.07	$-4.01^{+0.11}_{-0.09}$	$-3.74^{+0.09}_{-0.10}$
	43.21 ± 0.1	1.73	$-4.42^{+0.14}_{-0.11}$	$-4.10^{+0.10}_{-0.11}$
	43.41 ± 0.1	1.73	$-4.94^{+0.30}_{-0.18}$	$-4.60^{+0.14}_{-0.16}$
	43.61 ± 0.1	4.18	$-5.34^{+0.31}_{-0.18}$	$-4.97^{+0.14}_{-0.16}$
	43.81 ± 0.1	4.18	$-5.97^{+0.31}_{-0.26}$	$-5.51^{+0.20}_{-0.26}$